Version of Record: https://www.sciencedirect.com/science/article/pii/S0926337322000546
Manuscript_f2794d4705a00a6209b136888b424400

$(La_{0.8}Sr_{0.2})_{0.98}MnO_{3-\delta}$-$Zr_{0.92}Y_{0.16}O_{2-\delta}$:$PrO_x$ for Oxygen Electrode Supported Solid Oxide Cells

Tianrang Yang[1,2], Shannon L. Kollasch[1], Jerren Grimes[1], Alan Xue[1], Scott A. Barnett[1]*

1. Department of Materials Science and Engineering, Northwestern University, Evanston, Illinois 60208, USA

2. Key Laboratory of Power Station Energy Transfer Conversion and System (North China Electric Power University), Ministry of Education, Beijing 102206, China

*Corresponding author: s-barnett@northwestern.edu

Abstract

$(La_{0.8}Sr_{0.2})_{0.98}MnO_{3-\delta}$ (LSM)- $Zr_{0.92}Y_{0.16}O_{2-\delta}$ (YSZ) has been widely studied as the cathode for solid oxide fuel cells (SOFCs), but its low activity has been a cell performance limiting factor. Herein, LSM-YSZ:PrO_x composite is developed as an active electrocatalyst for both oxygen reduction and evolution reactions. A single step PrO_x infiltration into LSM-YSZ lowers the polarization resistance (R_p) 10-20 times depending on the test temperature. Distribution of relaxation times (DRT) calculation reveals that adding PrO_x affects surface exchange between adsorbed/desorbed oxygen and lattice oxygen, and oxygen dissociative adsorption/desorption. A symmetrical cell with a thin YSZ electrolyte sandwiched between thick LSM-YSZ:PrO_x electrode-supports is developed and its oxygen generation performance and stability are evaluated under various current densities and temperatures. Reversible solid oxide cell (ReSOC) performance is also reported for LSM-YSZ:PrO_x supported cells with the oxide fuel electrode $Sr_{0.95}(Ti_{0.3}Fe_{0.63}Ni_{0.07})O_{3-\delta}$ (STFN).

Keywords: solid oxide cells; oxygen generators; oxygen electrode; infiltration; LSM-YSZ

Introduction

Solid oxide cells (SOCs) studied to date have mostly utilized a relatively thick electrolyte or fuel-electrode as the physical support of the cells. The other option is to use a thick oxygen electrode as the support, but such cells have not been more widely developed due to the difficulty of co-firing the electrolyte (typically YSZ) and oxygen electrode; since the temperature required to densify the electrolyte is relatively high, problems with electrode/electrolyte reactions and over-densifying the electrode can occur. Nonetheless, a method for achieving high performance electrodes via co-firing of oxygen electrode supports with a YSZ electrolyte would help enable new device configurations with unique applications. One such application is the electrochemical oxygen generator that can produce high-purity pressurized oxygen.[1] By using co-firing, cells with a thin YSZ electrolyte can be made with symmetric supporting oxygen electrodes, ideal for extracting pure oxygen from air. An advantage of this device compared to the mixed-conducting high-temperature membranes, that have been extensively developed for producing pure oxygen for combustion processes in order to produce sequestration-ready CO_2,[2] is that oxygen transport across the membrane is driven electrochemically, instead of by an applied pressure. Indeed, electrochemical pressurization of oxygen from ambient air is possible.

Another application is for reversible SOCs. The reversible solid oxide cell (ReSOC) is an energy conversion device that electrolyzes H_2O and CO_2 to produce fuels (e.g., H_2, CO, CH_4) that can be stored indefinitely, and then generates electricity in fuel cell mode using the stored fuels.[3, 4] Electricity storage via ReSOCs is particularly important for application in concert with intermittent renewable sources (solar and wind); storage capacity must be increased significantly in order to allow increasing penetration of renewable electrical sources.[5] A key characteristic of ReSOCs is the capability to do long-term storage of large amounts of energy when used in a system

with large capacity gas storage. [6] Compared to fuel-electrode- supported ReSOC designs, oxygen-electrode supported cells have the advantage of a relatively thin fuel electrode that minimizes the concentration polarization that can arise during electrolysis with low steam content or fuel cell operation with low hydrogen content. If the fuel electrode is Ni-YSZ, making it thinner improves the tolerance of the cell to volume change during redox cycles.[7] Since the fuel electrode can be fired after electrolyte sintering, lower temperatures can be utilized enabling the use of alternative fuel-electrode materials that cannot be co-fired at electrolyte sintering temperature; this could be important because the main degradation mechanisms in solid oxide cells (e.g., poor redox cycling stability,[8] deactivation of Ni by coking when working with hydrocarbon fuels,[9] coarsening[10] and Ni migration during electrolysis[11]) are associated with the nominal Ni-YSZ fuel electrode. Although oxygen binary diffusion (in air) in a relatively thick oxygen electrode support is a disadvantage for conventional solid oxide fuel cells, this problem can be alleviated in the ReSOC application by feeding the oxygen electrode with pure oxygen, produced during previous electrolysis operation cycle, during fuel cell operation.[12]

Although there has been some success in preparing oxygen electrode supported cells, e.g., with LSM-YSZ and YSZ electrolyte,[13-15] performance is typically inferior to fuel-electrode supported cells because of the non-ideal microstructure of the oxygen electrode.[15] One way to overcome this difficulty is via the use of infiltration, as demonstrated in a recent report where cell performance was improved via $Sr(Ti,Fe.Co)O_3$ infiltration.[16] PrO_x infiltrated into various electrode scaffolds generally yields very low polarization resistance, e.g., PrO_x coated Gd-doped Ceria (GDC),[17] $PrBa_{0.5}Sr_{0.5}Co_{1.5}Fe_{0.5}O_{5+\delta}$,[18], $La_{0.6}Sr_{0.4}Co_{0.2}Fe_{0.8}O_{3-\delta}$ (LSCF)-GDC,[19] $SrTi_{0.3}Fe_{0.63}Co_{0.07}O_{3-\delta}$,[20] but has not been utilized in oxygen electrode supported cells, to our knowledge.

Here we report on two types of SOCs based on PrO_x-infiltrated LSM-YSZ oxygen-electrode supports and YSZ electrolytes: LSM-YSZ:PrO_x,O_2 | YSZ | LSM-YSZ: PrO_x,O_2 oxygen generators and LSM-YSZ:PrO_x,O_2 | YSZ | $Sr_{0.95}(Ti_{0.3}Fe_{0.63}Ni_{0.07})O_{3-\delta}$:fuel reversible SOCs. PrO_x infiltration into the LSM-YSZ substantially decreases the oxygen electrode polarization resistance. The $Sr_{0.95}(Ti_{0.3}Fe_{0.63}Ni_{0.07})O_{3-\delta}$ (STFN) fuel electrodes provide an alternative to Ni-YSZ that has previously shown promising performance resulting from exsolved Ni-Fe alloy particles.[21] The symmetrical cells are studied with electrochemical impedance spectroscopy (EIS). EIS fitting results are obtained using equivalent circuits developed with the aid of distribution of relaxation times (DRT) analysis combined with microstructural observations. The symmetrical cell results also provide a means to directly observe the impacts of PrO_x on LSM-YSZ performance. Results of symmetric cell life tests, where the cells operate like oxygen generators, are presented and cell stability is discussed. ReSOC performance results are also presented.

Experimental

Cell fabrication

Oxygen-electrode-support (OES) symmetrical cells were prepared by tape casting, hot-press lamination and cofiring. The compositions for OES layer and functional layer are 38.5 wt.% LSM (Praxair) + 41.5 wt.% YSZ (Tosoh) + 8 wt.% starch (pore former) + 12 wt.% Graphite (pore former), and 38.5 wt.% LSM + 38.5 wt.% YSZ + 23 wt.% Graphite (pore former), respectively. The YSZ electrolyte contained 3% mol Fe_2O_3 as the sintering aid. After lamination, the green pellets were co-fired at 1250 °C for 4 h to obtain the final symmetrical cells. The active area was 1.75 cm^2. The thickness of OES layer, functional layer and electrolyte layer are 400, 10 and 16 μm, respectively.

For full SOCs, OES half-cells were first prepared, followed by screen printing $Gd_{0.1}Ce_{0.9}O_{2-\delta}$ (GDC, FuelcellMaterials) buffer layer and firing at 1200 ºC for 2h. STFN was then screen printed on the GDC and fired at 1050 ºC for 3 h. STFN powder was prepared with solid state reaction using the raw materials $SrCO_3$ (Sigma-Aldrich), TiO_2 (Alfa Aesar), Fe_2O_3 (Alfa Aesar,), and $Ni(NO_3)_2{\cdot}6H_2O$ (Sigma-Aldrich). Powders were mixed with amounts yielding the composition $Sr_{0.95}(Ti_{0.3}Fe_{0.63}Ni_{0.07})O_{3-\delta}$ and ball milled in ethanol for 24 hours, dried, and calcined at 1100 °C for 10 hours. The resulting powder was ball milled again in ethanol for another 48 hours and dried to obtain the final powder. The inks for screen-printing were prepared by mixing the powder with vehicle (V-737, Heraeus) with weight ratio of 1:1.2 in a three-roll mill. The electrode active area was 0.5 cm^2. The thickness of OES layer, functional layer, YSZ layer, GDC layer and STFN layer are 400, 10, 8, 3 and 10 μm, respectively.

The infiltration solution was prepared by adding 1:2 molar ratio $Pr(NO_3)_3{\cdot}6H_2O$ (Sigma-Aldrich) and citric acid (Sigma-Aldrich) into de-ionized water. 2 weight percent of Triton X-100 was added as surfactant. Electrodes were infiltrated once with 20 μL solution, dried at 60 ºC for 5h, then fired at 450 °C for 0.5 h. The loading amounts were *ca.* 1wt% and 2wt% PrO_2 for 1 M and 2 M Pr-ion solution, respectively.

Characterization

Current collector grids were screen printed onto the electrodes: silver (Heraeus) on LSM-YSZ and gold (Heraeus) on STFN. EIS spectra were collected using an IM6 Electrochemical Workstation (ZAHNER, Germany) with a 20 mV AC signal in the frequency range of from 0.1 Hz to 100 kHz (under OCV condition) in stagnant air. For single cell tests, the cells were sealed onto alumina tubes with silver paste (DAD-87, Shanghai Research Institute of Synthetic Resins). An 100 sccm flow of humidified H_2 (50% H_2-50% H_2O) was supplied to fuel electrode side while

150 sccm air was supplied to the oxygen electrode side. IV curves were measured at 20 mV increments over the relevant voltage ranges for fuel cell and electrolysis operation. The EIS spectra were collected under same settings as for symmetrical cells. Galvanostatic life testing was conducted with a Keithley 2400 source/load measure unit. DRT calculations for EIS spectra were performed with DRT tools, a GUI implemented in MATLAB[22]. The EIS fittings were conducted with home-developed Python code. PyEIS was used as a reference during the code development.[23]

X-ray diffraction (XRD) data were collected on pure CuKα1 radiation (STOE STADI-P) at a scan rate of 5°/min. The XRD samples were prepared by mixing LSM, YSZ or $Pr(NO_3)_3 \cdot 6H_2O$ in a mortar with a weight ratio of 5:5:2, corresponding to 7.95wt% PrO_x (calculation basis PrO_2). The higher PrO_x concentration in XRD sample than the actual cells are used for two reasons: 1) the concentration of PrO_x phase is for sure above the detection limit of XRD. 2) excessive PrO_x can offer enough reactants for the reactions between LSM-YSZ and PrO_x, if any. Cell microstructures were examined via scanning electron microscopy SEM (Hitachi SU8030).

Results and discussion

Phase compatibility

Figure 1 shows room temperature XRD patterns for LSM-YSZ with or without PrO_x, after annealing in air at 900 °C for 40 h. This test was done at higher temperature than the typical cell operating temperature (≤ 800 C) in order to produce any materials interactions that might occur during the longer operating times typical of SOCs. The expected LSM, YSZ, and PrO_x phases are observed, but no secondary phases. PrO_x is present as PrO_2 (cubic) in this measurement, made after cooling the cell to room temperature; however, a number of homologous compounds with a general

composition Pr_nO_{2n-2}, e.g., Pr_2O_3 and PrO_2, (corresponding to n=4 and ∞, respectively) may have been present when the cell was still at high temperature.[24] Since PrO_x is observed as a separate phase, there is no evidence of significant reaction between PrO_x and LSM-YSZ.

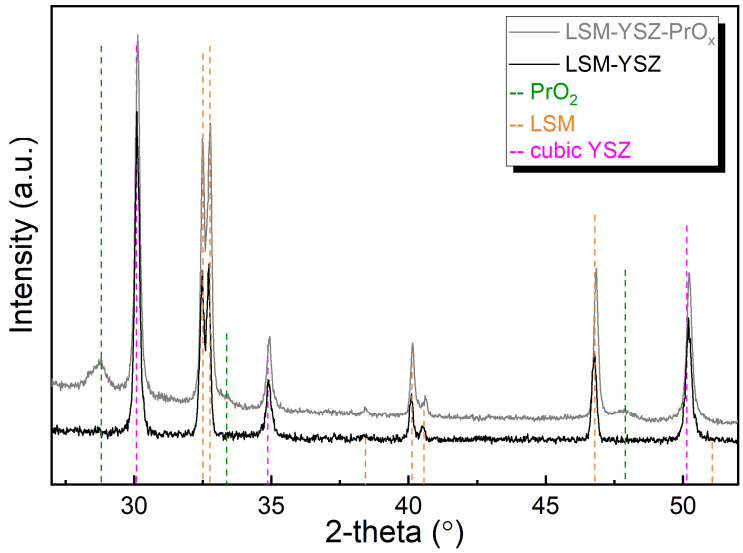

Figure 1. XRD patterns of LSM-YSZ with or without PrO_x after annealing at 900 °C for 40 h. The PDF# for PrO_2, LSM and cubic YSZ are 75-0077, 89-0648 and 30-1468, respectively.

Electrochemical Characteristics – Symmetric Cells

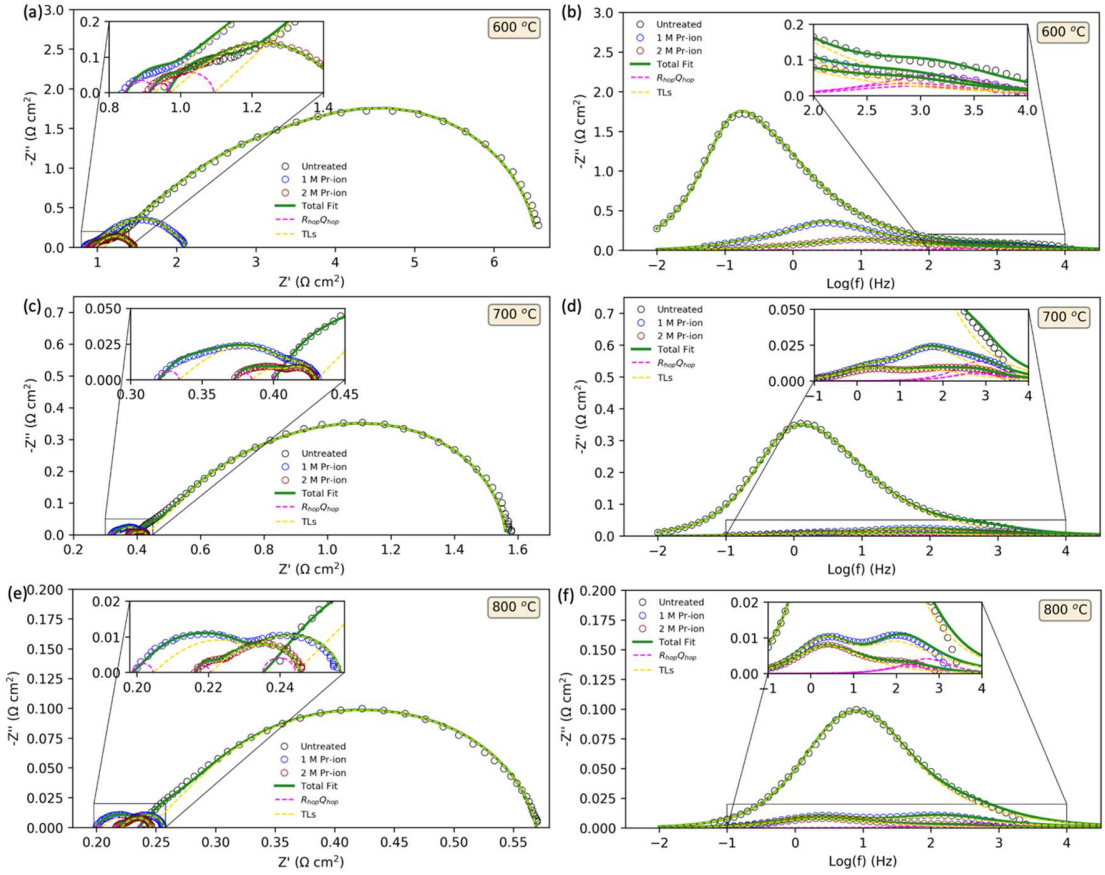

Figure 2. The EIS spectra and fitting curves for symmetrical cells at (a) (b) 600, (c) (d) 700 and (e) (f) 800 ºC. (a), (c), and (e) are Nyquist plots; (b), (d), and (f) are Bode plots. These results were all obtained in the early stages (within ~ 0.5 h after initial heating) of cell testing.

Figure 2 shows the EIS spectra taken at various temperatures from cells without Pr infiltration (LSM-YSZ:0), with 1M Pr-ion infiltration (LSM-YSZ:1M), and 2M Pr-ion infiltration (LSM-YSZ:2M). There are substantial differences in the shape of the EIS arcs, suggesting changes in relative contributions of various electrode processes. In order to explore this, DRT analysis was carried out that suggested four main processes in LSM-YSZ:0, denoted as P1, P2, P3 and P4 going from high to low frequency (**Figure 3a**). Multiple electrode processes have been identified in LSM-YSZ electrodes, including from high to low frequency: (1) oxygen species hopping across

the LSM/YSZ interfaces within the electrode and oxygen ions hopping from the electrode into the YSZ electrolyte lattice,[25, 26] (2) ionic conduction in YSZ in the electrode,[25, 27] (3) surface exchange reactions (oxygen dissociative adsorption/desorption and charge transfer)[25, 26, 28], and (4) gas diffusion[25, 29]. For LSM-YSZ:0, P1 and P2 are presumably associated with processes (1) and (2), respectively. On the other hand, P3 and P4 are probably associated with process (3). The dominant process P4 varies strongly with temperature, and hence it is clearly not gas diffusion.[28, 29] Its frequency at ~ 1 Hz is consistent with the oxygen dissociative adsorption/desorption process.[30-32]. Hence, P3 is likely the response from the charge transfer at LSM surface. In previous reports, P3 and P4 have been treated as one integrated process due to their overlap, modeled either as a resistance and a constant phase element (CPE) in parallel (RQ)[29, 33] or a transmission line model (Gerischer element)[32, 34]. Adding PrO_x is beneficial for all the processes while the presence of PrO_x virtually eliminates P4 and largely reduces the size of P3, indicating its fast oxygen dissociative adsorption/desorption and charge transfer capabilities.

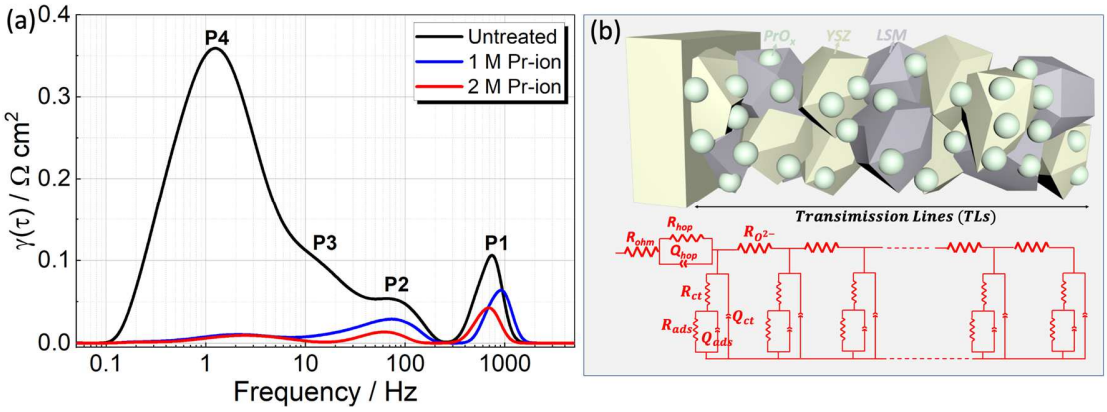

Figure 3. (a) DRT plots derived from EIS spectra of symmetrical cells measured in air at 700 °C. (b) Schematic of equivalent circuit model for EIS spectra fittings.

An equivalent circuit (**Figure 3b**) including a transmission line model (TLM) was used for the EIS spectra fittings. The P1 process is simulated with a resistor (R_{hop}) and constant phase capacitor Q_{hop} in parallel. The P2, P3 and P4 processes are simulated with the TLM, in which $R_{O^{2-}}$, R_{ct}, and R_{ads} represent oxygen-ion conduction, charge transfer, and oxygen adsorption/desorption resistances, respectively; Q_{ct} and Q_{ads} are used to simulate the capacitive character of the corresponding processes. L denotes the electrode thickness. The fitting curves are shown along with the EIS spectra in **Figure 2** and the fitting resistance values are plotted in **Figure 4**. The ohmic resistance (R_{ohm}) exhibits the expected temperature dependence, while the slight differences between the cells are likely due to slight variations in electrolyte thickness. The infiltration drastically reduces the total polarization resistance R_p. At 700 °C, for example, R_p = 0.057 Ω cm^2 for LSM-YSZ:2M compared to 0.114 Ω cm^2 for LSM-YSZ:1M and 1.18 Ω cm^2 for LSM-YSZ:0. R_{ct} and R_{ads} are reduced by a factor of 10 – 1000 for the PrO_x-infiltrated electrodes; this is reasonable since these processes are known to be fast on PrO_x,[20, 35] and these processes can occur over the entire PrO_x surface area as opposed to LSM-YSZ, where reactions occur only near three-phase boundaries. R_{hop} is ~ 5 times smaller after infiltration, suggesting that PrO_x significantly enhances the oxygen-ion transport beyond that due to the YSZ phase in the electrode. All of the resistances in **Figure 4** exhibit an Arrhenius behavior at lower temperatures. For higher temperatures, however, R_{ads} and R_{ct} appear to saturate for the infiltrated samples above 650 °C.

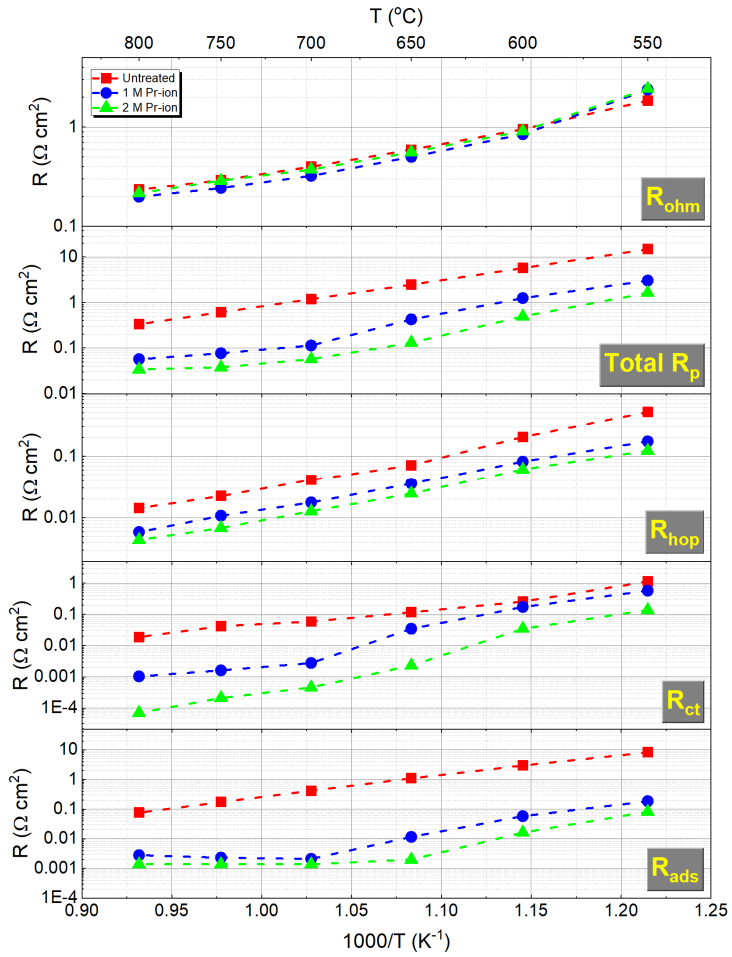

Figure 4. Fitted values of ohmic, total polarization, hopping, charge transfer, and adsorption resistances plotted versus inverse temperature for symmetric cells with un-infiltrated, 1 M Pr-ion, and 2 M Pr-ion infiltrated LSM-YSZ electrodes.

Symmetric cell life test results and analysis

Two different types of life test results are described here: testing at high temperature without current to probe the stability of infiltrated nano-scale PrO_x, and testing over a range of current densities to test for possible degradation caused by high current.

High temperature life test without current

Figure 5 shows the life test results for symmetric cells with LSM-YSZ:0, LSM-YSZ:1M, and LSM-YSZ:2M electrodes without current at 800 ºC. As seen in **Figure 5a**, R_{ohm} increases during the first ~ 100 h for all three samples, presumably initial electrode conditioning, but stabilizes after that. The rapid increase of R_p for LSM-YSZ:0 during the first ~ 100 h is primarily due to an increase in R_{ads}, as R_{hop} and R_{ct} are quite stable (**Figure 5b-e**). Hence, the fast initial conditioning is likely a result of the surface property variation, such as oxygen vacancy quantity or segregated surface species considering their important roles in the surface exchange process of LSM.[36, 37] The gradual degradation in the later period may be a result of reduced three-phase boundary length caused by particle coarsening.[38, 39] For both infiltrated samples, increasing the amount of PrO_x yields lower initial R_p values, and while R_p increases throughout the test, the values remain substantially lower than for LSM-YSZ:0, e.g., 3 times lower for LSM-YSZ:2M. Much of the infiltrated electrode degradation results from a rapid increase in R_{ct}, which approaches the value for LSM-YSZ:0 after 1000 h at 800 ºC. R_{hop} and R_{ads} also both increase with time, but remain lower than that of LSM-YSZ:0.

The SEM images in **Figure 6** suggest a morphology transition of PrO_x from initially discrete surface nanoparticles on LSM-YSZ surfaces to flatter surfaces with barely discernable surface particles. The morphology evolution might be driven by good wettability between PrO_x and the LSM-YSZ substrate, causing the PrO_x particles to spread out over the electrode surfaces, yielding a smoother surface with substantially lower surface area. Also, a small fraction of the Pr may diffuse into LSM and/or YSZ during the life test. The morphology changes of PrO_x particles largely reduce the effective electrode surface area, which inevitably causes the increase of R_{ads} and R_{ct} since they are area-specific processes. The observation that the 2M Pr-ion infiltrated electrode

degrades less shows that a higher initial density of nanoparticles helps to preserve electrode activity.

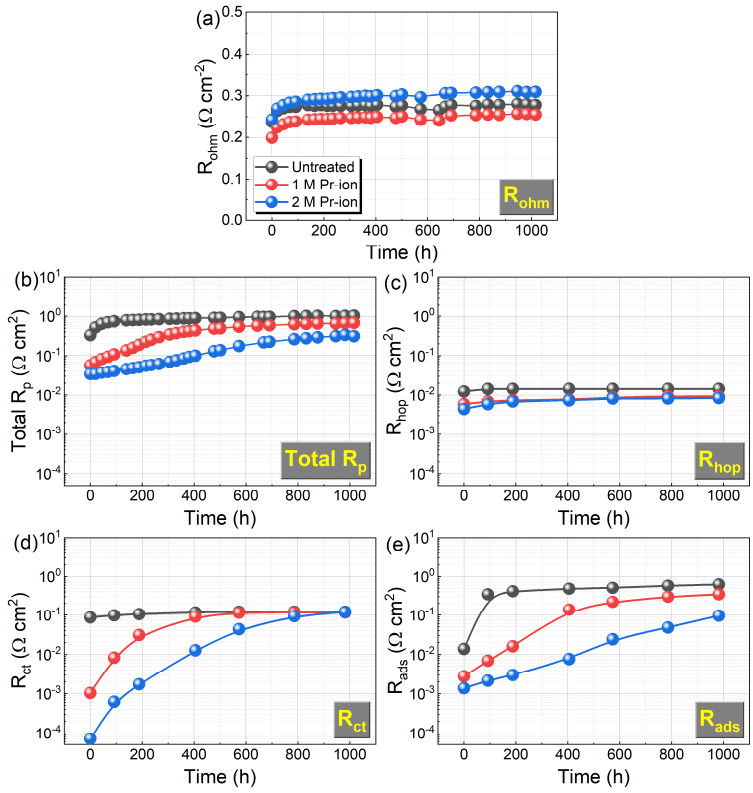

Figure 5. Time-dependent (a) R_{ohm}, (b) R_p, (c) R_{hop}, (d) R_{ct} and (e) R_{ads} at 800 ºC for LSM-YSZ:0, LSM-YSZ:1M and LSM-YSZ:2M symmetrical cells.

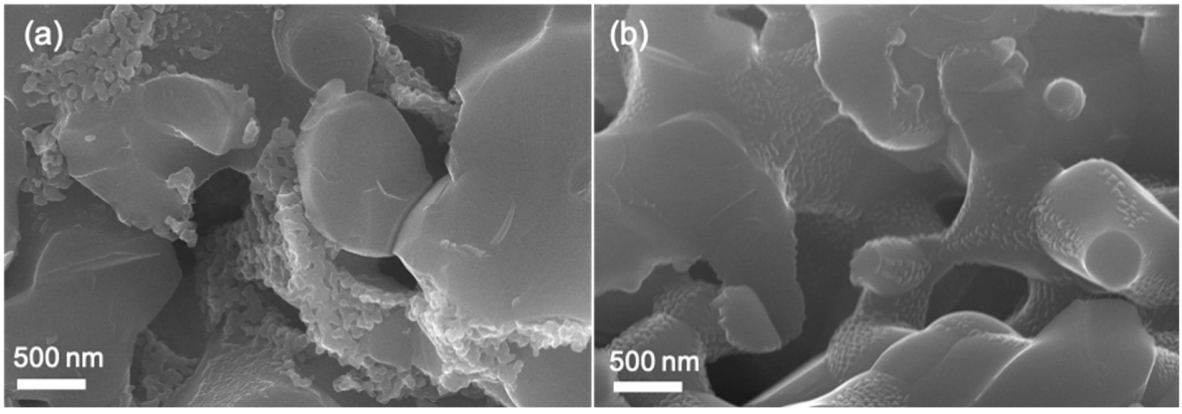

Figure 6. SEM images of LSM-YSZ:2M symmetrical cell electrode after (a) annealing for 0.5 h and (b) the 1000 h life test at 800 ºC.

The present results can be compared with prior life tests of PrO_x-infiltrated electrodes, although these were done with different electrodes – LSCF and STFC - and at lower temperatures of 550 - 650 ^oC.[35] These showed a slight degradation of the electrode performance along with coarsening of PrO_x nanoparticles over 1000 h. The present life tests show a much larger loss of electrode performance and a bigger change in the PrO_x surface morphology; although the different electrode materials in those tests may have had an impact on the results, it seems likely that the accelerated performance degradation in the present results was a result of the higher temperature.

Low-temperature life test with current density

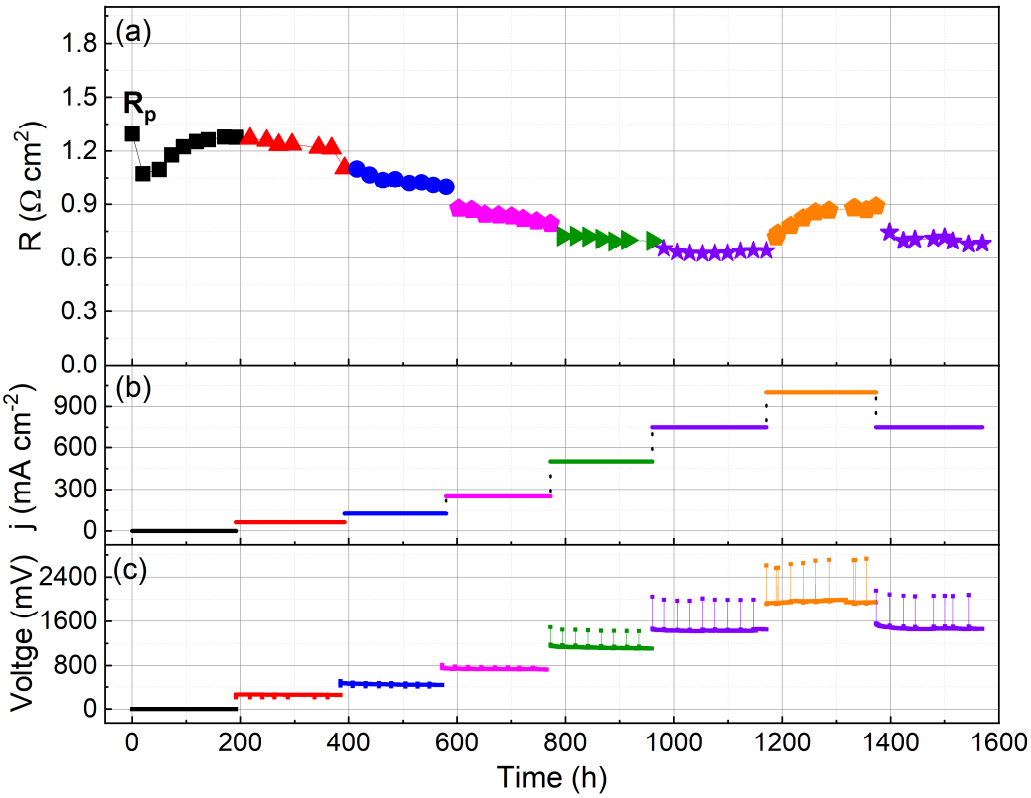

Figure 7. Life test results for LSM-YSZ:2M symmetrical cell with *ca.* 200 h-stepwise current flows from 0-1000 mA cm^{-2} at 600 ^oC. Time-dependent (a) R_p at OCV, (b) current density and (c) voltage profiles.

Figure 7 shows the life test result for a symmetric cell with LSM-YSZ:2M carried out at different current densities for 1569 h at 600 °C. In this case, the cell is operating effectively as an oxygen pump. During the initial period at zero current, R_p varies rapidly before stabilizing. The initial drop might arise from the better current collection or surface conditioning after temperature ramping, while the gradual increase after that might be caused by the interactions between different phases or particles coarsening. Then, after this initial conditioning period, operation with increasing current density causes a decrease in R_p. LSM-based electrodes are known for their current activation behavior, resulting from the increase of oxygen vacancy concentration and/or the decrease of segregated passivation species at the electrode surface.[40-43] After R_p appears to become fairly stable at 750 mA cm^{-2}, increasing the current to 1000 mA cm^{-2} causes a resistance increase. However, R_p decreases again when the current is later decreased back to 750 mA cm^{-2}, indicating that there is no permanent damage, e.g., electrode delamination, to the cell. The fitted resistance values for the last EIS spectra at each current density are plotted in **Figure 8**. The fitting results indeed show that the decrease of R_p during 0-750 mA cm^{-2} is mainly a result of improved charge transfer and oxygen adsorption/desorption, consistent with the current activation behavior of LSM.[40, 41] Stable R_p is obtained during the later stage at 750 mA cm^{-2} with a value of 0.64 Ω cm^2. The total cell ASR is as low as 1.49 Ω cm^2 after nearly 1200 h at 600 °C. The reversibility of R_p on going from 750 to 1000 and back to 750 mA cm^{-2} also comes from the surface exchange process, as seen from the reversibility of R_{ct} and R_{ads} in **Figure 8**. The regeneration of LSM-YSZ electrode activity has been reported previously after switching the current direction (anodic-to-cathodic) because of the incorporation of the passivating SrO at LSM surface,[40] or improved contact at LSM/YSZ interfaces,[41] which might also occur when the DC current dropping from 1000 to 750 mA cm^{-2}.

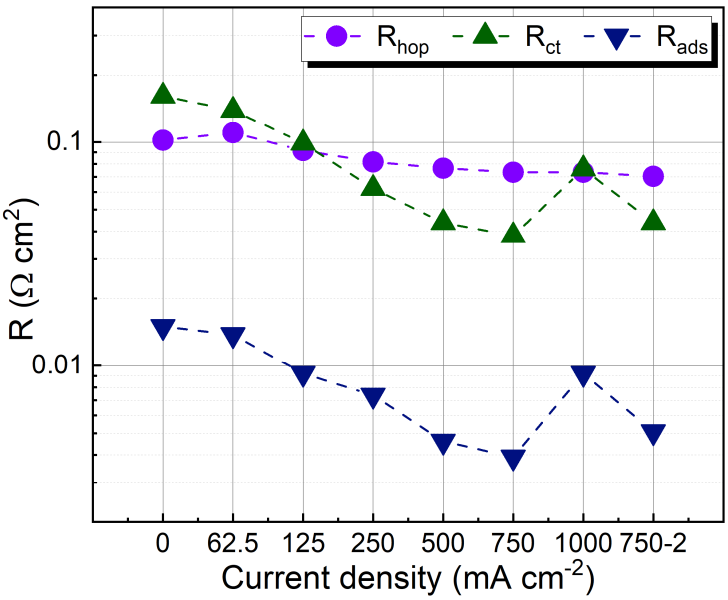

Figure 8. The fitted polarization resistance values for the last EIS spectra at each current density.

When LSM-YSZ is operated as an electrolysis anode at high current density, it can degrade via delamination, it can degrade due to a relatively high electrode overpotential (η); higher η means higher effective oxygen pressure at the electrode/electrolyte interface. [44, 45] The DRT plots for the EIS at various current densities in **Figure 9a** show that the electrode process is mainly limited by charge transfer (P3). In this case, η can be estimated using an approximate form of the Butler-Volmer equation [45]:

$$\eta = \frac{2RT}{zF} sinh^{-1}(\frac{j}{2j_0}) \quad (1)$$

where R is gas constant, F is the Faraday constant, and z is the charge transferred in the relevant reaction. The exchange current density j_0 in eq. 1 can be related to the measured R_p value using:

$$j_0 = \frac{RT}{zFR_p} \quad (2)$$

The last measured R_p value at each current density is used for calculation, yielding η_{th} = 192.1 and 238.1 mV at 750 and 1000 mA cm^{-2}, respectively (**Figure 9b**). A threshold η for void formation is 222 mV at 600 °C for YSZ electrolyte.[45] The post-test SEM in **Figure 10** shows that more voids are present at the oxygen evolution reaction (OER) side than the oxygen reduction reaction (ORR) side, which will lead to delamination if continuing the current test at 1000 mA cm^{-2}.

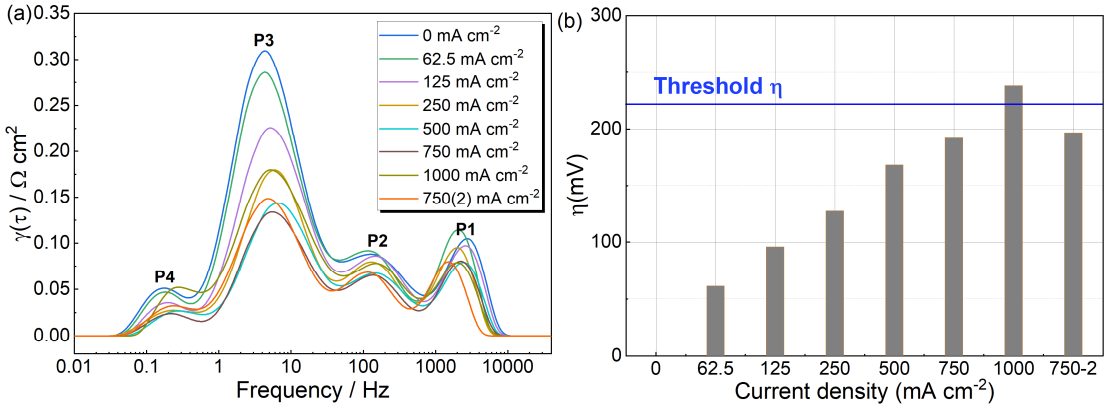

Figure 9. (a) The DRT plots for the last EIS spectra at each current density and (b) calculated η values with eqs.1.

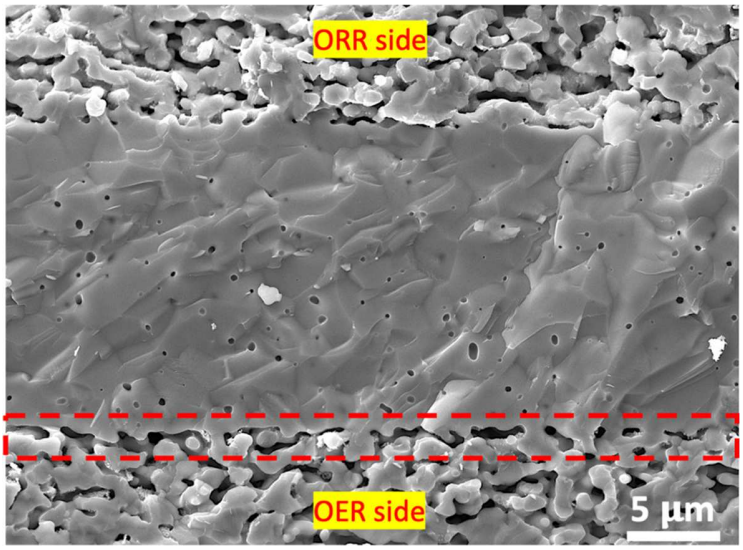

Figure 10. The cross-section SEM after life test for LSM-YSZ:2M symmetrical cell at 600 °C.

Note that LSM-YSZ electrolysis anodes normally degrade by delamination at a current density of 1 A cm^{-2} at 800 °C, due to a too-high electrode overpotential. The calculated overpotential under the same condition for the LSM-YSZ:2M electrode here is only 33.4 mV, which is significantly lower than the threshold for degradation. The PrO_x infiltration yields a remarkable improvement in electrode stability, keeping the overpotential low enough to avoid serious degradation at 600 °C – a full 200 °C lower temperature!

Reversible SOC performance

Figure 11a shows the current-voltage curves for full cells with the LSM-YSZ:0 or LSM-YSZ:2M oxygen-electrode and STFN fuel-electrode at 700 and 750 °C. The peak power density at 700 °C in fuel cell mode increases from 0.15 to 0.39 W cm^{-2} with 97%H_2-3%H_2O as fuel after infiltration. Although this power density is not as high as some fuel-electrode-supported cells, the cell with infiltrated electrode is amongst the best reported oxygen-electrode-supported cells under these conditions (see Table 1). The ReSOC performance was also tested for the infiltrated cell with 50%H_2-50%H_2O as fuel. The electrolysis current reaches 0.59 A cm^{-2} at a thermal neutral voltage of 1.3 V at 750 °C (**Figure 11b**).

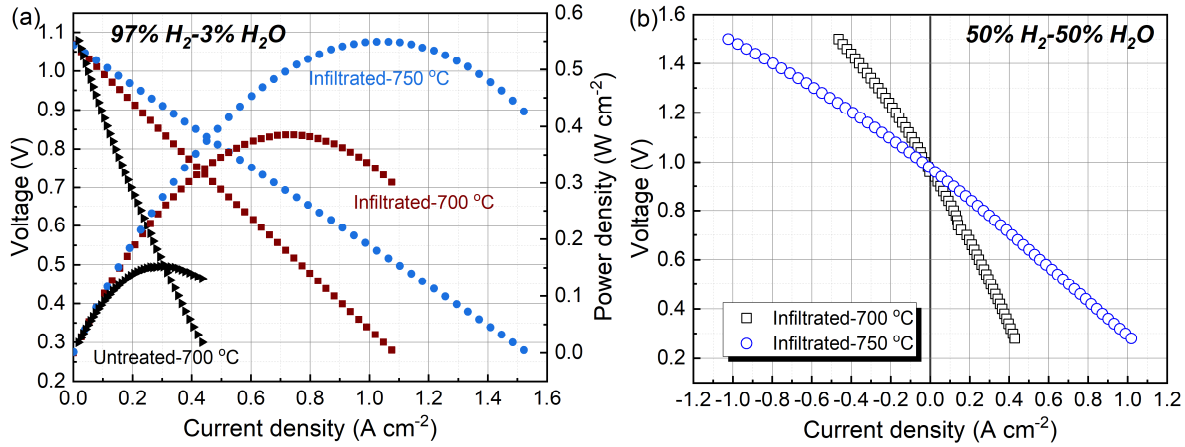

Figure 11. IV curves for oxygen-electrode supported full cells with LSM-YSZ or LSM-YSZ:PrO_x oxygen electrodes tested in (a) 97%H_2-3%H_2O or (b) 50%H_2-50%H_2O fuel.

Table 1. Peak power densities (PPDs) for oxygen-electrode supported fuel cells with thin electrolyte membrane reported in the literature at 700 °C under 97%H_2-3%H_2O and air (unless otherwise noted).

Oxygen-electrode	Electrolyte	Fuel-electrode	PPDs (W cm^{-2})	Refs
LSM-YSZ	YSZ(15 μm)	Ni-YSZ	0.36(850 °C)	[46]
LSM-SDC	SDC/YSZ(20 μm)	Ni-SDC	0.58(850 °C, pure O_2)	[47]
LSM-SDC	SSZ(30 μm)	Ni-SDC	0.23(800 °C)	[48]
LSM-YSZ:GDC	YSZ(10 μm)	Ni-YSZ	0.22(750 °C)	[13]
YSZ:LSFSc	YSZ(20 μm)	Ni-SDC	0.57(750 °C)	[49]
LSM-SSZ	SSZ(15 μm)	Ni-SSZ	0.33(750 °C)	[50]
LSM-YSZ	YSZ(27 μm)	LSCM	0.18 (750 °C)	[51]
LSM-YSZ	YSZ(27 μm)	Ni-YSZ	0.06	[14]
LCCMNCr:SDC	SCSZ(60 μm)	Ni-SCSZ	0.18	[52]
LSC-GDC	LSGM/SDC	Ni-GDC	0.22	[53]
PNSM-SDC	SDC(10 μm)/YSZ(5 μm)	Ni-SDC	0.29	[54]
LSM-YSZ:SDC	YSZ(13 μm)	Ni-YSZ	0.29	[15]
LSM-YSZ:STFC	YSZ(10 μm)/GDC(3μm)	STFN	0.31	[16]
LSM-YSZ:STFC	YSZ(10 μm)/GDC(3μm)	STFR	0.40	[16]
YSZ:LSF	YSZ(15 μm)	Cu–SDC:CeO_2	0.33	[55]
LSM-YSZ:PrO_x	YSZ(8 μm)/GDC(3μm)	STFN	0.39	This work

Note: SDC: $Ce_{0.8}Sm_{0.2}O_{2-\delta}$; SSZ: $Zr_{0.9}Sc_{0.1}O_{2-\delta}$; LSFSc: $La_{0.6}Sr_{0.4}Fe_{0.9}Sc_{0.1}O_{3-\delta}$; LSCM: $La_{0.75}Sr_{0.25}Cr_{0.5}Mn_{0.5}O_{3-\delta}$; LCCMNCr: $La_{0.6}Ca_{0.3}Ce_{0.1}Mn_{1-x-y}Ni_xCr_yO_{3-\delta}$ ($x + y < 0.01$); SCSZ: $Sc_{0.1}Ce_{0.01}Zr_{0.89}O_{2-\delta}$; LSGM: $La_{0.9}Sr_{0.1}Ga_{0.8}Mg_{0.2}O_{3-\delta}$; PNSM: $Pr_{0.35}Nd_{0.35}Sr_{0.3}MnO_{3-\delta}$; STFC: $SrTi_{0.3}Fe_{0.6}Co_{0.1}O_{3-\delta}$; STFR: $SrTi_{0.3}Fe_{0.63}Ru_{0.07}O_{3-\delta}$; LSF: $La_{0.8}S_{0.2}FeO_{3-\delta}$.

Conclusions

Single step PrO_x infiltration is shown to substantially reduce the polarization resistance of LSM-YSZ oxygen electrodes, e.g., by more than 20 times at 700 °C with 2 M Pr-ion solution infiltration. Analysis of impedance spectroscopy results indicates that adding PrO_x improves the surface exchange between the adsorbed/desorbed oxygen and lattice oxygen, along with the

oxygen dissociative adsorption/desorption rates. An LSM-YSZ:PrO_x supported solid oxide cell with thin YSZ electrolyte and STFN fuel electrode yields state-of-the-art fuel cell performance.

For the LSM-YSZ:PrO_x supported symmetrical cells with thin YSZ electrolyte, the R_p value of the 2 M Pr-ion infiltrated sample degrades slower than the 1 M Pr-ion infiltrated cell at 800 ^oC, maintaining an R_p value ~ 3 times lower than that of LSM-YSZ over 1000 h. The degradation of LSM-YSZ:PrO_x mainly comes from the charge transfer and oxygen dissociative adsorption/desorption processes, indicating a diminished activity of infiltrated PrO_x particles over time. A more stable R_p value is obtained during extended cell operation at a lower temperature, even under high current density. During cell operation at 600 ^oC, gradually increasing the current density yields a decrease in R_p, reaching a value of 0.64 Ω cm^2 at 750 mA cm^{-2} after 1000 h operation. Degradation occurs only when the current density reaches 1000 mA cm^{-2}, where the anode overpotential exceeds a critical value for electrode fracture. Compared to LSM-YSZ alone, where the overpotential is large enough to cause degradation even at 800 ^oC, PrO_x yields a remarkable improvement in the range of stable operation. The symmetric cells could be promising for application in oxygen generation devices.

CRediT authorship contribution statement

Tianrang Yang: Conceptualization, Methodology, Investigation, Software, Data collection and curation, Visualization, Writing - original draft. **Shannon L. Kollasch**: Investigation, Data collection, Formal analysis. **Jerren Grimes**: Investigation. **Alan Xue**: Investigation. **Scott A. Barnett**: Funding acquisition, Conceptualization, Methodology, Supervision, Writing - review & editing.

Declaration of Competing Interest

The authors report no declarations of interest.

Acknowledgements

This work is supported by the Office of Energy Efficiency and Renewable Energy, US Department of Energy (DE-EE0008437).

References

[1] P.A.B. Sadashiv Swami, Richard Martin Kelly, Oxygen supply method and apparatus, Praxair Technology Inc, United States, 2012.
[2] J. Sunarso, S. Baumann, J. Serra, W. Meulenberg, S. Liu, Y. Lin, J.D. Da Costa, Mixed ionic–electronic conducting (MIEC) ceramic-based membranes for oxygen separation, Journal of membrane science, 320 (2008) 13-41.
[3] N.Q. Minh, M.B. Mogensen, Reversible solid oxide fuel cell technology for green fuel and power production, The Electrochemical Society Interface, 22 (2013) 55.
[4] W. Zhang, Y. Zhou, E. Liu, Y. Ding, Z. Luo, T. Li, N. Kane, B. Zhao, Y. Niu, Y. Liu, A highly efficient and durable air electrode for intermediate-temperature reversible solid oxide cells, Applied Catalysis B: Environmental, 299 (2021) 120631.
[5] U.S. Department of Energy, Energy Storage Grand Challenge Roadmap, 2020.
[6] S.H. Jensen, C. Graves, M. Mogensen, C. Wendel, R. Braun, G. Hughes, Z. Gao, S.A. Barnett, Large-scale electricity storage utilizing reversible solid oxide cells combined with underground storage of CO_2 and CH_4, Energy & Environmental Science, 8 (2015) 2471-2479.
[7] K. Yamahara, C.P. Jacobson, S.J. Visco, L.C. De Jonghe, Catalyst-infiltrated supporting cathode for thin-film SOFCs, Solid State Ionics, 176 (2005) 451-456.
[8] S. Tao, J.T. Irvine, A redox-stable efficient anode for solid-oxide fuel cells, Nature materials, 2 (2003) 320-323.
[9] W. Wang, C. Su, Y. Wu, R. Ran, Z. Shao, Progress in solid oxide fuel cells with nickel-based anodes operating on methane and related fuels, Chemical reviews, 113 (2013) 8104-8151.
[10] Y.-c.K. Chen-Wiegart, D. Kennouche, J. Scott Cronin, S.A. Barnett, J. Wang, Effect of Ni content on the morphological evolution of Ni-YSZ solid oxide fuel cell electrodes, Applied Physics Letters, 108 (2016) 083903.
[11] X. Sun, P. Hendriksen, M. Mogensen, M. Chen, Degradation in solid oxide electrolysis cells during long term testing, Fuel Cells, 19 (2019) 740-747.
[12] S.-L. Zhang, H. Wang, T. Yang, M.Y. Lu, S.A. Barnett, Characteristics of Oxygen Electrode Supported Reversible Solid Oxide Cells, Journal of The Electrochemical Society, 168 (2021) 054504.

[13] S.U. Rehman, R.-H. Song, J.-W. Lee, T.-H. Lim, S.-J. Park, S.-B. Lee, Effect of GDC addition method on the properties of LSM–YSZ composite cathode support for solid oxide fuel cells, Ceramics International, 42 (2016) 11772-11779.
[14] X. Meng, N. Yang, X. Gong, Y. Yin, Z.-F. Ma, X. Tan, Z. Shao, S. Liu, Novel cathode-supported hollow fibers for light weight micro-tubular solid oxide fuel cells with an active cathode functional layer, Journal of Materials Chemistry A, 3 (2015) 1017-1022.
[15] L. Sun, N. Li, C. Chen, Z. Zhan, Comparative study of solid oxide fuel cells supported on ceramic cathodes with different pore structures, International Journal of Hydrogen Energy, 46 (2021) 13330-13339.
[16] S.-L. Zhang, H. Wang, T. Yang, M.Y. Lu, C.-X. Li, C.-J. Li, S.A. Barnett, Advanced oxygen-electrode-supported solid oxide electrochemical cells with $Sr(Ti,Fe)O_{3-\delta}$-based fuel electrodes for electricity generation and hydrogen production, Journal of Materials Chemistry A, 8 (2020) 25867-25879.
[17] C. Nicollet, A. Flura, V. Vibhu, A. Rougier, J.-M. Bassat, J.-C. Grenier, An innovative efficient oxygen electrode for SOFC: Pr_6O_{11} infiltrated into Gd-doped ceria backbone, international journal of hydrogen energy, 41 (2016) 15538-15544.
[18] Y. Chen, B. deGlee, Y. Tang, Z. Wang, B. Zhao, Y. Wei, L. Zhang, S. Yoo, K. Pei, J.H.Kim, Y. Ding, P. Hu, F.F. Tao, M. Liu, A robust fuel cell operated on nearly dry methane at 500° C enabled by synergistic thermal catalysis and electrocatalysis, Nature Energy, *3*(2018) 1042-1050.
[19] B.-K. Park, S.A. Barnett, Boosting solid oxide fuel cell performance via electrolyte thickness reduction and cathode infiltration, Journal of Materials Chemistry A, 8 (2020) 11626-11631.
[20] J. Grimes, S.A. Barnett, Effect of Pressurization on Solid Oxide Cell Oxygen Electrodes: the Role of PrO_x Nanoparticle Infiltration, Journal of The Electrochemical Society, 168 (2021) 084514.
[21] T. Zhu, H.E. Troiani, L.V. Mogni, M. Han, S.A. Barnett, Ni-substituted $Sr(Ti,Fe)O_3$ SOFC anodes: achieving high performance via metal alloy nanoparticle exsolution, Joule, 2 (2018) 478-496.
[22] T.H. Wan, M. Saccoccio, C. Chen, F. Ciucci, Influence of the Discretization Methods on the Distribution of Relaxation Times Deconvolution: Implementing Radial Basis Functions with DRTtools, Electrochimica Acta, 184 (2015) 483-499.
[23] K.B. Knudsen, Pyeis: A Python-Based Electrochemical Impedance Spectroscopy Analyzer and Simulator, Meeting Abstracts, The Electrochemical Society, 2019, pp. 1937-1937.
[24] V. Thangadurai, R.A. Huggins, W. Weppner, Mixed ionic-electronic conductivity in phases in the praseodymium oxide system, Journal of Solid State Electrochemistry, 5 (2001) 531-537.
[25] M.J. Jørgensen, M. Mogensen, Impedance of solid oxide fuel cell LSM/YSZ composite cathodes, Journal of the Electrochemical Society, 148 (2001) A433.
[26] L.C. Baqué, P.S. Jørgensen, W. Zhang, K.V. Hansen, M. Søgaard, Effect of aging on the electrochemical performance of LSM-YSZ cathodes, Journal of The Electrochemical Society, 162 (2015) F971.
[27] R. Wang, Z. Sun, Y. Lu, S. Gopalan, S.N. Basu, U.B. Pal, Comparison of chromium poisoning between lanthanum strontium manganite and lanthanum strontium ferrite composite cathodes in solid oxide fuel cells, Journal of Power Sources, 476 (2020) 228743.

[28] J. Nielsen, J. Hjelm, Impedance of SOFC electrodes: A review and a comprehensive case study on the impedance of LSM: YSZ cathodes, Electrochimica Acta, 115 (2014) 31-45.
[29] E.P. Murray, T. Tsai, S.A. Barnett, Oxygen transfer processes in (La,Sr)MnO_3/Y_2O_3-stabilized ZrO_2 cathodes: an impedance spectroscopy study, Solid State Ionics, 110 (1998) 235-243.
[30] S.J. Xia, V.I. Birss, A kinetic study of the oxygen reduction reaction at $LaSrMnO_3$-YSZ composite electrodes, Journal of the Electrochemical Society, 152 (2005) A570.
[31] K. Chen, N. Ai, Enhanced electrochemical performance and stability of (La,Sr)MnO_3–(Gd, Ce)O_2 oxygen electrodes of solid oxide electrolysis cells by palladium infiltration, International journal of hydrogen energy, 37 (2012) 1301-1310.
[32] S.B. Adler, Factors governing oxygen reduction in solid oxide fuel cell cathodes, Chemical reviews, 104 (2004) 4791-4844.
[33] E. Lee, H. Jeong, T.H. Shin, J.-h. Myung, Determination of the rate-determining step of the oxygen reduction reaction of $La_{0.8}Sr_{0.2}MnO_3$ (LSM)-8mol% yttria-stabilized zirconia (YSZ): Composition and microstructure, Ceramics International, 47 (2021) 1792-1797.
[34] E.-C. Shin, P.-A. Ahn, H.-H. Seo, J.-M. Jo, S.-D. Kim, S.-K. Woo, J.H. Yu, J. Mizusaki, J.-S. Lee, Polarization mechanism of high temperature electrolysis in a Ni–YSZ/YSZ/LSM solid oxide cell by parametric impedance analysis, Solid State Ionics, 232 (2013) 80-96.
[35] M.Y. Lu, R. Scipioni, B.-K. Park, T. Yang, Y.A. Chart, S.A. Barnett, Mechanisms of PrO_x performance enhancement of oxygen electrodes for low and intermediate temperature solid oxide fuel cells, Materials Today Energy, 14 (2019).
[36] S. Piskunov, E. Heifets, T. Jacob, E.A. Kotomin, D.E. Ellis, E. Spohr, Electronic structure and thermodynamic stability of $LaMnO_3$ and $La_{1-x}Sr_xMnO_3$ (001) surfaces: Ab initio calculations, Physical Review B, 78 (2008) 121406.
[37] L. Wang, R. Merkle, Y.A. Mastrikov, E.A. Kotomin, J. Maier, Oxygen exchange kinetics on solid oxide fuel cell cathode materials-general trends and their mechanistic interpretation, J. Mater. Res., 27 (2012) 2000-2008.
[38] M. Brant, T. Matencio, L. Dessemond, R. Domingues, Electrical degradation of porous and dense LSM/YSZ interface, Solid State Ionics, 177 (2006) 915-921.
[39] T. Yang, J. Liu, Y. Lei, W. Li, T.-L. Cheng, H. Finklea, Y.-H. Wen, X. Liu, H.W. Abernathy, S. Lee, Investigation of LSM-YSZ Composite Cathode Performance Degradation with a Multistep Charge Transfer Model, Journal of The Electrochemical Society, 166 (2019) F448.
[40] A.-K. Huber, M. Falk, M. Rohnke, B. Luerßen, L. Gregoratti, M. Amati, J. Janek, In situ study of electrochemical activation and surface segregation of the SOFC electrode material $La_{0.75}Sr_{0.25}Cr_{0.5}Mn_{0.5}O_{3\pm\delta}$, Physical Chemistry Chemical Physics, 14 (2012) 751-758.
[41] K. Chen, S.-S. Liu, N. Ai, M. Koyama, Why solid oxide cells can be reversibly operated in solid oxide electrolysis cell and fuel cell modes?, Physical Chemistry Chemical Physics, 17 (2015) 31308-31315.
[42] S.P. Jiang, Activation, microstructure, and polarization of solid oxide fuel cell cathodes, Journal of Solid State Electrochemistry, 11 (2007) 93-102.
[43] S. McIntosh, S.B. Adler, J.M. Vohs, R.J. Gorte, Effect of polarization on and implications for characterization of LSM-YSZ composite cathodes, Electrochem Solid St, 7 (2004) A111.
[44] G.A. Hughes, J.G. Railsback, K.J. Yakal-Kremski, D.M. Butts, S.A. Barnett, Degradation of $(La_{0.8}Sr_{0.2})_{0.98}MnO_{3-\delta}$–$Zr_{0.84}Y_{0.16}O_{2-\gamma}$ composite electrodes during reversing current operation, Faraday discussions, 182 (2015) 365-377.

[45] B.-K. Park, Q. Zhang, P.W. Voorhees, S.A. Barnett, Conditions for stable operation of solid oxide electrolysis cells: oxygen electrode effects, Energy & Environmental Science, 12 (2019) 3053-3062.
[46] T. Liu, J. Lin, H. Wu, C. Xia, C. Chen, Z. Zhan, Tailoring the pore structure of cathode supports for improving the electrochemical performance of solid oxide fuel cells, J Electroceram, 40 (2018) 138-143.
[47] M. Chen, J.-L. Luo, K.T. Chuang, A.R. Sanger, Fabrication and electrochemical properties of cathode-supported solid oxide fuel cells via slurry spin coating, Electrochimica acta, 63 (2012) 277-286.
[48] G. Chen, H.-X. You, Y. Kasai, H. Sato, A. Abudula, Characterization of planer cathode-supported SOFC prepared by a dual dry pressing method, Journal of alloys and compounds, 509 (2011) 5159-5162.
[49] C. Yuan, T. Luo, J. Li, X. Meng, J. Qian, X. Ye, Z. Zhan, C. Xia, S. Wang, Infiltrated porous YSZ as a cathode active layer for cathode-supported solid oxide fuel cells, Electrochemistry communications, 46 (2014) 40-43.
[50] C. Yuan, Y. Liu, Y. Zhou, Z. Zhan, S. Wang, Fabrication and characterization of a cathode-support solid oxide fuel cell by tape casting and lamination, International journal of hydrogen energy, 38 (2013) 16584-16589.
[51] X. Chen, Q. Liu, S. Chan, N. Brandon, K.A. Khor, High-performance cathode-supported SOFC with perovskite anode operating in weakly humidified hydrogen and methane, Fuel Cells Bulletin, 2007 (2007) 12-16.
[52] X. Li, N. Xu, X. Zhao, K. Huang, Performance of a commercial cathode-supported solid oxide fuel cells prepared by single-step infiltration of an ion-conducting electrocatalyst, Journal of Power Sources, 199 (2012) 132-137.
[53] L. Peng, X. Yan, H. You, Preparation and performance optimization of intermediate temperature cathode-supported SOFC, IOP Conference Series: Materials Science and Engineering, IOP Publishing, 2018, pp. 012026.
[54] M. Liu, D. Dong, F. Zhao, J. Gao, D. Ding, X. Liu, G. Meng, High-performance cathode-supported SOFCs prepared by a single-step co-firing process, Journal of Power Sources, 182 (2008) 585-588.
[55] L. Zhao, X. Ye, Z. Zhan, High-performance cathode-supported solid oxide fuel cells with copper cermet anodes, Journal of Power Sources, 196 (2011) 6201-6204.

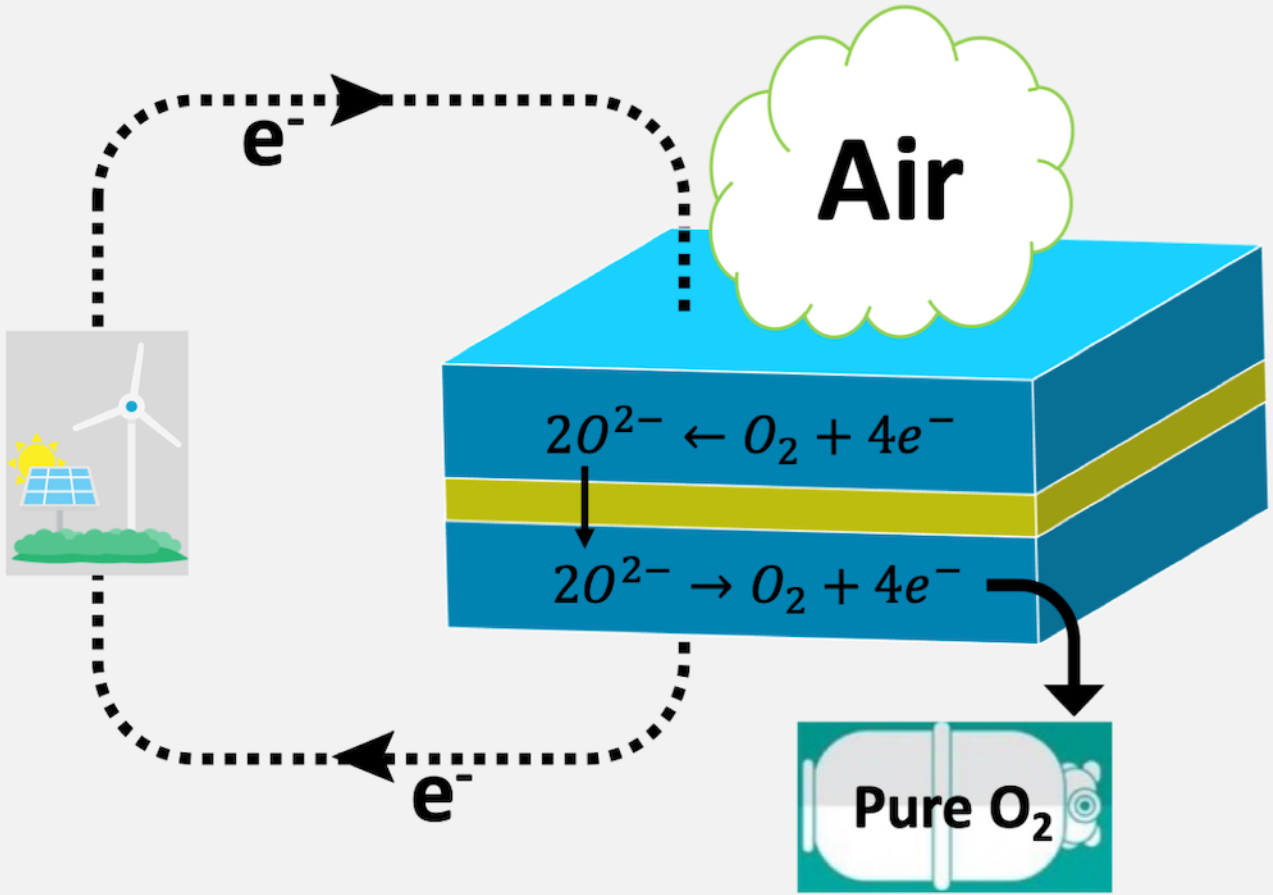
e-
Air
$2O^{2-} \leftarrow O_2 + 4e^-$
$2O^{2-} \rightarrow O_2 + 4e^-$
e-
Pure O_2

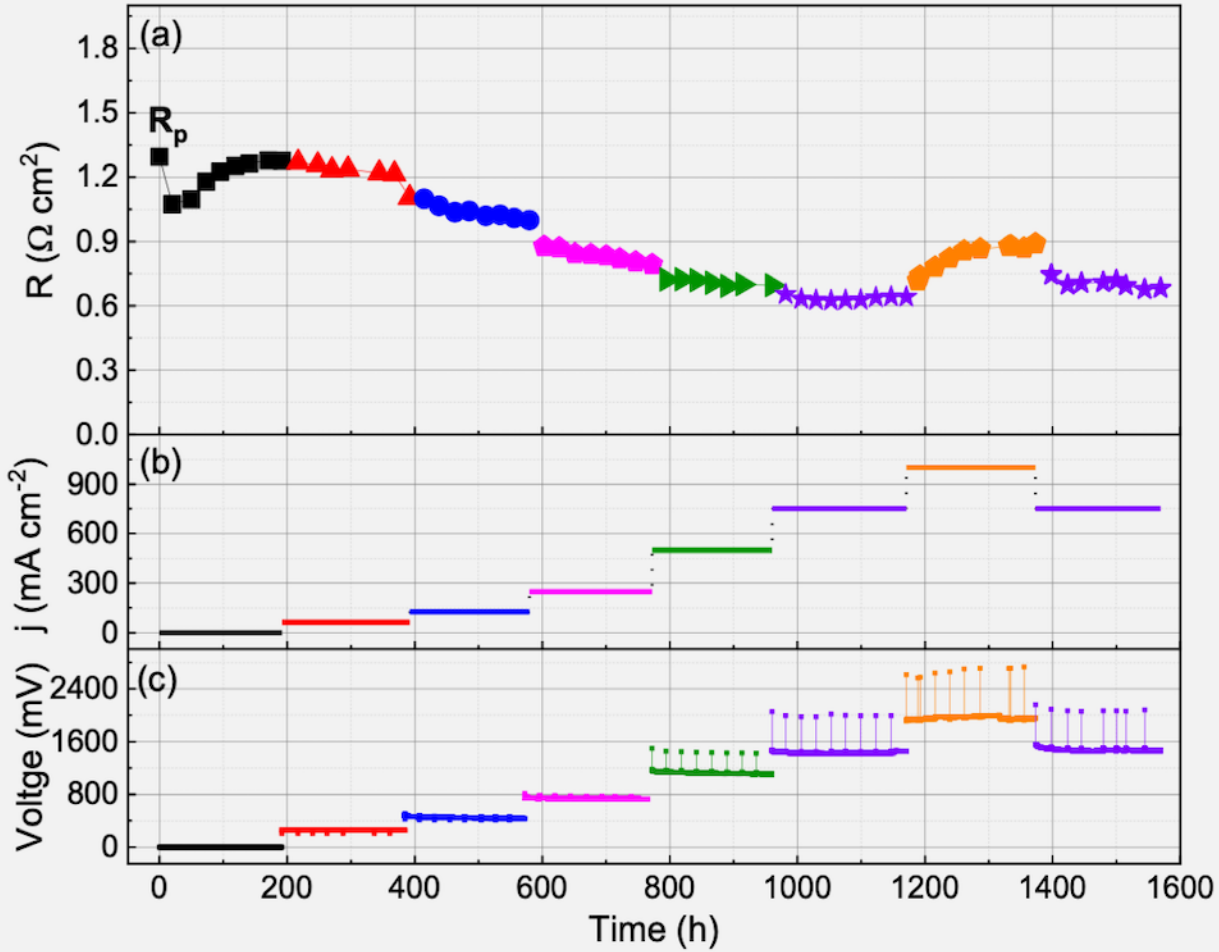
(a)
R_p
R (Ω cm²)
1.8
1.5
1.2
0.9
0.6
0.3
0.0
(b)
j (mA cm⁻²)
900
600
300
0
(c)
Voltge (mV)
2400
1600
800
0
0
200
400
600
800
1000
1200
1400
1600
Time (h)